Control of gain and thermal carrier loss profiles for mode optimization in 980-nm broad-area vertical-cavity surface-emitting lasers*

Wu Jian(吴 坚)†, Cui Huai-Yang(崔怀洋), Huang Meng(黄 梦), and Ma Ming-Lei(马明磊)

Department of Applied Physics, Beihang University, Beijing 100191, *China*

(Received 29 January 2013; revised manuscript received 13 March 2013)

Optical gain and thermal carrier loss distributions regarding current diffusion and various electric contact areas are investigated to improve the near-field modes from the ring-shape to a Gaussian-like configuration for extra-broad-area and oxide-confined vertical-cavity surface-emitting lasers. In this work an equivalent circuit network model is used. The resistance of the continuously-graded distributed Bragg reflectors (DBRs), the current diffusion and the temperature effect due to different electric-contact areas are calculated and analyzed at first, as these parameters affect one another and are the key factors in determining the gain and thermal carrier loss. Finally, the gain and thermal carrier loss distributions are calculated and discussed.

Keywords: optical gain, carrier loss, thermal effect, vertical-cavity-surface-emitting laser

PACS: 42.55.Px, 73.40.Kp, 73.40.Cg **DOI:** 10.1088/1674-1056/22/12/124203

1. Introduction

A general way to increase optical output power of a single vertical-cavity surface-emitting laser (VCSEL) diode is to use a broad-area device, in view of an extremely thin active region of the VCSEL. However, the problem from the use of the broad-area VCSEL is the difficulty of achieving a single transverse mode output, as a ring-shaped distribution of the injection current density with lower values in the central zone and higher values around the side of the active region usually occurs due to the current crowding effect at the border of the oxide-confined current aperture that is fairly near to the active region in the device. This ring-shaped carrier density configuration will cause optical gain and thermal carrier loss to vary in a similar distribution to it and finally result in high-order ring-mode formation.[1,2]

The fact that there exist mutual influences among the distributed Bragg reflector (DBR) resistances, the current diffusion, the temperature effect, the gain, and the carrier loss in the VCSEL, and that the current distribution in the active region is directly related to the geometric sizes of both electric contacts of the VCSEL, offer the possibility of improving the ring-mode situation in the broad-area VCSEL device by controlling the gain and thermal carrier loss distributions using different electric-contact areas. As is well known, the enhancement of the current density in the central zone of the active region can increase the gain in this zone by reducing the p-contact area for the broad-area bottom-emitting VCSEL. However, this processing will induce the temperature to increase in the same zone due to the DBR ohm heating, and thus, additional thermal carrier loss occurs from quantum wells. So these are two conflicting processes in the mode control and it is also difficult to obtain the thermal carrier leakage loss distribution in the active region by either experimental measurement or theoretical modeling.

Regarding the transverse mode investigation on the VCSEL, most previous papers focused on the small-area VCSEL devices (normally < 20 μm in diameter), in which the fundamental mode was able to be achieved, owing to the optimization and control of guiding effects. The gain distribution did not play a dominant role in the mode control for such small devices. Thus, the radial current diffusion in the active region was commonly assumed to be a Gaussian-like or a top-hat function, or described by solving the Poisson's equation of the current in the mode analysis.[2–7] However, these previous studies were not suitable for the extra-broad-area VCSELs (> 300 μm in diameter), in which the gain and carrier loss distributions could play a more important role in the mode formation and control, apart from the guiding effect.[8–12] So far, only a few papers have analyzed either the influence of various electric contact areas on current distribution,[13] or the influences of the current, temperature, gain, and wave-guiding on the modes.[14] Unfortunately, the former failed to further describe spatial gain and carrier loss variations by taking into account the temperature effect induced by the current diffusion. The latter did not describe the gain and thermal carrier loss distributions by changing the contact area in the mode control.

Thus, in order to control the gain and thermal carrier loss profiles to improve the ring-mode situation in the extra-broad-

*Project supported by the National Natural Science Foundation of China (Grant No. 10974012).

†Corresponding author. E-mail: jwu2@buaa.edu.cn

© 2013 Chinese Physical Society and IOP Publishing Ltd

area VCSEL, in this paper, we establish an equivalent circuit network model consisting of a series of resistors and diodes for the bottom-emitting VCSEL to characterize the current transportation and diffusion in the VCSEL with various p-contact areas at first. Then, the temperature effect related to the current distribution in the active region is modeled using a three-dimensional (3D) finite element model and the stable-state thermal conduction equation based on the DBR resistance calculation. Finally, the gain and the thermal carrier loss distributions from different p-contact areas for the ring-mode control are calculated and discussed.

2. Calculation model

The extra-broad-area oxide-confined 980-nm VCSEL structure for the modeling is based on the experimental sample as shown in Fig. 1.

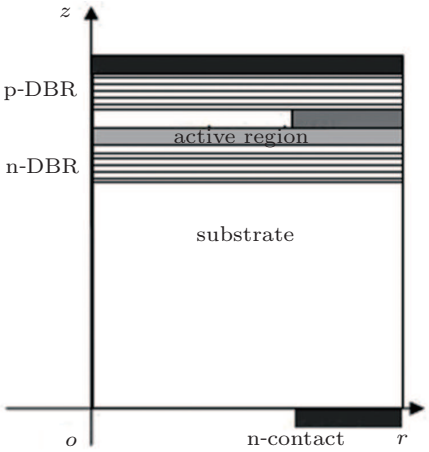


Fig. 1. Diagram of the 980-nm oxide-confined bottom-emitting VCSEL structure.

The top and bottom DBR reflectors consist of 30 periods of the continuously-graded p-type $Al_xGa_{1-x}As/Al_{1-x}Ga_xAs$ materials with a thickness of 0.02 μm per layer ($0.1 \leq x \leq 0.9$, carbon-doping concentration: 2.5×10^{18} cm^{-3}) and 28-periods of the continuously-graded n-type $Al_xGa_{1-x}As/Al_{1-x}Ga_xAs$ materials with a thickness of 0.02 μm per layer ($0.1 \leq x \leq 0.9$, silicon-doping concentration: 2.0×10^{18} cm^{-3}), respectively. The active region consists of two $Ga_{0.8}In_{0.2}As$ quantum wells, between which a $GaAs_{0.92}P_{0.08}$ layer is sandwiched. The oxide-confined current aperture is 600 μm in diameter. The overall structure is grown on the GaAs substrate. The *P–I–V* characteristics of the VCSEL sample are given in Fig. 2.

An equivalent circuit network model for characterizing electric characteristics of the VCSEL is built by referring to the SPICE-like model[4,6] and shown in Fig. 3. In Fig. 3, five nodes in the radial direction and nine nodes in the axial direction are drawn for the principle illustration here. More nodes are involved in the actual calculation. In this model, the VCSEL is first cut into N_h annular elements in the radial direction, and then sliced into N_v layers in the axial direction. The lateral resistor $R_{h(ij)}$ represents the resistance between the two annular elements neighboring each other in the same layer. The vertical resistor $R_{v(ij)}$ denotes the resistance between the two layers neighboring each other in the same annular element. The diode $D_{(ij)}$ is used for describing the electric characteristics of the quantum well in the active region. Every sliced layer in both DBRs consists of a pair of $Al_xGa_{1-x}As/Al_{1-x}Ga_xAs$ layers each with a thickness of d.

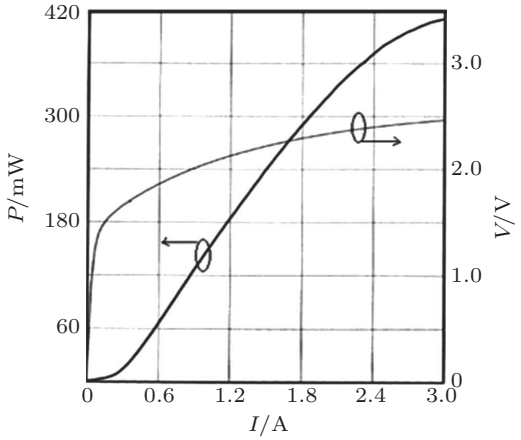


Fig. 2. *P–I–V* characteristics of the extra-broad-area and bottom-emitting 980-nm VCSEL with an oxide-confined current aperture of 600 μm in diameter.

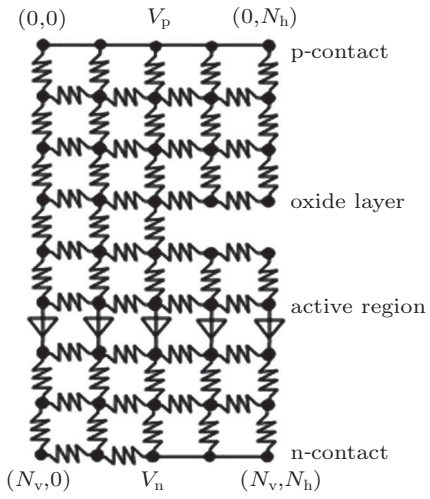


Fig. 3. Diagram of the circuit network model of the VCSEL structure.

3. Current diffusion

In order to determine the resistances and the current diffusion in the network, the axial junction resistances of both graded $Al_xGa_{1-x}As/Al_{1-x}Ga_xAs$ DBR reflectors are calculated using the thermionic emission model and the finite difference method,[15–18] as the series junction resistances of both DBRs play a dominant role in the temperature effect. The differential junction resistances corresponding to the reverse- and

forward-bias voltages for one pair of DBR layers can be determined by[18,19]

$$\rho'_{\mathrm{f,r}} = \left[\frac{q^2 N_{\mathrm{b}}}{kT}\left(\frac{kT}{2\pi m^*_{\mathrm{h}}}\right)^{1/2}\right]^{-1} \exp\left[\frac{q\,(V_{\mathrm{Db}} \mp V_{\mathrm{b}})}{kT}\right], \quad (1)$$

where V_{b} and V_{Db} are the applied voltage and the built-in voltage on the broad-bandgap side of the isotype hetero-junction formed between the DBR layers, N_{b} is the carrier concentration in the broad-bandgap side of the junction and approximately equal to the impurity concentration in the materials, and m^*_{h} denotes the effective mass of the holes. The detailed calculations on the differential junction resistances of both p- and n-type continuously-graded DBR reflectors for the 980-nm broad-area VCSEL may refer to our other paper.[18]

In addition to the axial junction resistances from both DBR reflectors, the radial and axial material resistances, $R_{h(ij)}$ and $R_{v(ij)}$ of the i-th annular element in the j-th layer are calculated by the following equations, according to the definition of material resistance:

$$R_{h(ij)} = \rho\frac{(r_{i+1} - r_i)}{\pi(r_{i+1} + r_i)d},$$
$$i = 0,1,2,\ldots,N_{h-1}, \quad j = 0,1,2,\ldots,N_{v-1}, \quad (2)$$
$$R_{v(ij)} = \rho\frac{d}{\pi(r^2_{i+1} - r^2_i)},$$
$$i = 0,1,2,\ldots,N_{h-1}, \quad j = 0,1,2,\ldots,N_{v-1}, \quad (3)$$

where ρ denotes the resistivity of the material. After the overall resistances are determined, the electric potential and current at each node of the circuit network can be obtained by the iterative calculation of the equations given above, in terms of the Kirchhoff's law. The calculation process for the potential and current at every node is illustrated below.

(i) The node potentials, excluding the active region which is treated as a group of forward-bias diodes whose resistances are omitted when the lasing is generated, are determined from the potential differences between two nodes adjacent to each other. So the current through a node may be determined by the following relation in terms of the Kirchhoff's law:

$$\frac{V_{i+1,j} - V_{i,j}}{R_{v(i,j)} + R_{s(i,j)}} - \frac{V_{i,j} - V_{i-1,j}}{R_{v(i,j)} + R_{s(i.j)}} - \frac{V_{i,j+1} - V_{i,j}}{R_{h(i,j)}} + \frac{V_{i,j} - V_{i,j+1}}{R_{h(i,j)}} = 0, \quad (4)$$

where $R_{s(i,j)}$ represents the junction resistance of the DBR layer.

(ii) The iterative calculation of the potentials is carried out with Eq. (4) and a computation program until the calculation result trends to the convergence within an error of less than 1.0×10^{-5} V.

(iii) The computation program starts with the parameters of the VCSEL sample and an initially-guessed low voltage. Then, the calculation process is repeated with higher voltages until a stable potential value is obtained. The computation flowchart is given in Fig. 4.

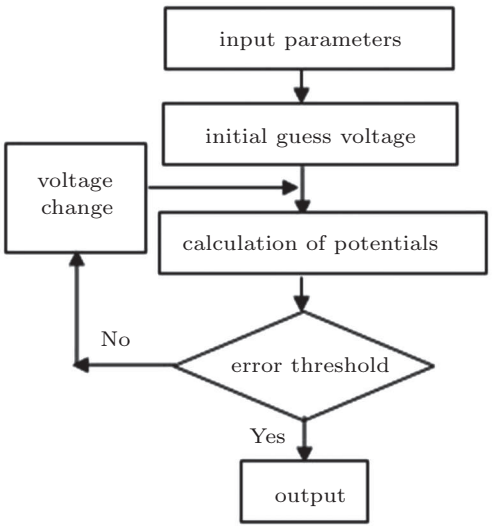


Fig. 4. Flowchart of iterative calculation on the electric potentials of the VCSEL.

The calculation results of the electric potentials around the DBR mirrors, the oxide-confined current aperture, and the active region with different p-contact diameters of 100 μm, 200 μm, 470 μm, and 1000 μm are plotted in Fig. 5.

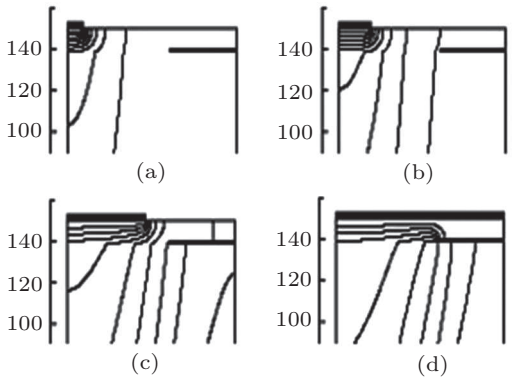


Fig. 5. Equal-potential lines around DBR mirrors, current aperture (600 μm in diameter), and active region with different p-contact diameters of (a) 100 μm, (b) 200 μm, (c) 470 μm, and (d) 1000 μm.

The applied voltage to the device is 2.5 V and the current aperture is 600 μm in diameter. This result clearly shows that the current crowding effect around the current aperture border will become more and more serious, as the p-contact area increases. The reason for this lies in the fact that there is a finite diffusion range of carriers in the radial direction for a certain injection carrier density. Thus, if the p-contact area of a bottom-emitting VCSEL is reduced, the equal-potential lines will shrink towards the center. It indicates that more injection carriers are concentrated in the central zone.

The effect of the p-contact area variation on the change of the current distribution in the active region of the bottom-emitting VCSEL can be illustrated by Fig. 6, obtained from

the iterative calculation mentioned above, where the p-contact is designed with five diameters of 20 μm, 100 μm, 200 μm, 470 μm, and 1000 μm for the given model with a fixed current aperture diameter of 600 μm to observe the current distribution variation.

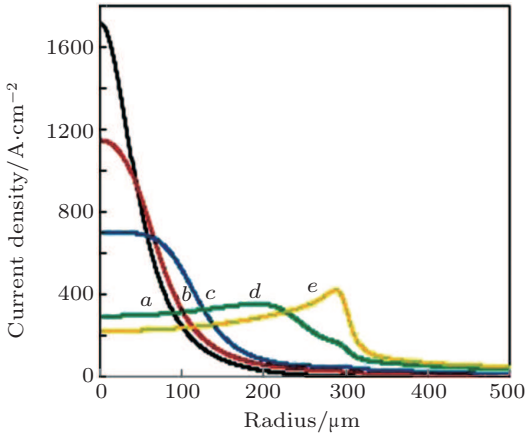


Fig. 6. (color online) Current diffusions in the active region with p-contact diameters of 20 μm (curve *a*), 100 μm (curve *b*), 200 μm (curve *c*), 470 μm (curve *d*), and 1000 μm (curve *e*). The current aperture is 600 μm.

The result shows that with the p-contact area decreasing, the peak of the current density shifts to the center, and when the p-contact is much smaller than the current aperture in diameter, e.g. a ratio of 20/600, the current density shows a Gaussian-like distribution. Nevertheless, this does not mean that the optical gain varies in the same form because the increase of the current density in the central zone of the active region would lead to higher temperature in the same zone due to the ohm heating, and thus, additional carrier leakage loss occurs from the wells so that the valid carrier numbers for recombination are reduced. Therefore, the temperature effect due to the current density variation is an important factor unable to be ignored in the optical gain and mode analysis. In order to obtain the correct spatial gain profile, the injected carrier density and the temperature must be considered together.

4. Temperature effect

Regarding the temperature effect in the VCSEL, the steady-state thermal conduction equation can be used here, that is,

$$\nabla^2 T + \frac{\dot{q}}{k} = 0, \tag{5}$$

where T denotes the temperature and k is the thermal conductivity, which is taken as $k = 0.28$ W/cm·K here for the GaAs-based materials,[20] $\dot{q}$ is the rate of total heat power generation per volume, which is mainly from the ohm heating contribution of the DBR reflectors of the VCSEL and can be expressed as the product of the injected current and the applied voltage to the device. Thus, the heating from the active region is omitted in the calculation as an approximation here. Both ambient and heat-sink temperatures are assumed to be $T_0 = 300$ K. The heat loss from the boundaries, exclusive of the top surface that is connected to the heat-sink, is calculated with the convection process. The calculation is completed using 3D finite element method in a cylindrical coordinate system. The temperature calculation results are shown in Fig. 7.

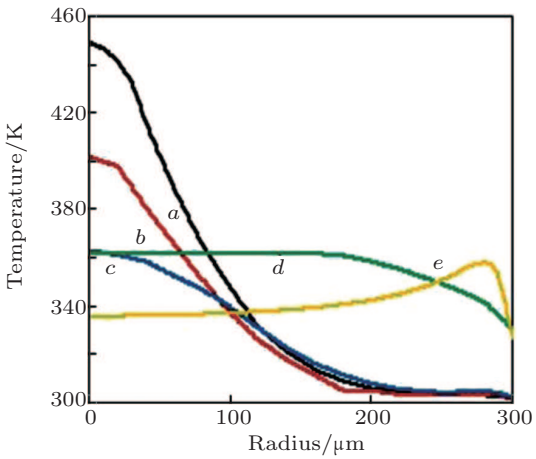


Fig. 7. (color online) Temperature distributions in the active region of the VCSEL from various p-contact diameters of 20 μm (curve *a*), 100 μm (curve *b*), 200 μm (curve *c*), 470 μm (curve *d*), and 1000 μm (curve *e*). The current aperture is 600 μm.

Obviously, as the p-contact area is reduced, the temperature in the central zone of the active region increases accordingly, due to the increased current density and ohm heating. Meanwhile, the temperature around the aperture side is apparently reduced. These temperatures show similar variations to the current densities in the radial direction.

5. Gain and carrier loss profiles

With the determination of both injection current density and temperature at each node of the circuit network using the iterative calculation and thermal conduction equation mentioned above, the spatial optical gain distribution in the active region may be obtained by the following relationship between the gain and the injection current:[21]

$$g = g_0 \ln \frac{J_{\rm in} + J_{\rm s}}{J_{\rm tr} + J_{\rm s}}, \tag{6}$$

where g_0 is the initial gain coefficient, $J_{\rm in}$ is the injection current density, $J_{\rm tr}$ is the transparency current density, and $J_{\rm s}$ is a small empirical constant. For the InGaAs quantum well, $g_0 = 1440$ cm^{-1}, $J_{\rm tr} = 50$ A/cm^2, and $J_{\rm s} = 1.0$ A·cm^{-2} under the room temperature here. Since there is a relationship of $g_0 \propto 1/T$ between the coefficient g_0 and the temperature,[21] the gain expression can be rewritten as

$$g = g_0 \left(\frac{300}{T}\right) \ln \frac{J + J_{\rm s}}{J_{\rm tr} + J_{\rm s}}. \tag{7}$$

Obviously, equation (7) should be more reasonable, as the gain is certainly reduced with the increase of temperature due to thermal carrier leakage loss from the wells for a fixed injection current level.

Substituting the results of the current and temperature calculations, which are shown in Figs. 6 and 7, into Eqs. (6) and (7), respectively, the optical gain distributions with and without the consideration of temperature influence from various p-contact areas are obtained as shown in Figs. 8 and 9, respectively.

The gains in Fig. 8 show similar profiles to those in Fig. 9, but the gain peaks in Fig. 8 are restricted due to the temperature-induced carrier loss from the well. Both Figs. 8 and 9 show that when the p-contact is larger than the current aperture in diameter, a typical ring-shaped gain distribution with a lower value in the center and a higher value around the side occurs. The gain peak is at $r = 300$ μm. This situation is not apparently changed, even if the p-contact area is slightly less than the current aperture due to the increased heating in the central zone. However, the gain peak has started to shift towards the center. The ring radius of the gain is reduced to 200 μm. This result means that the ring-shape of the mode still exists, but can be reduced in diameter. When the p-contact is considerably reduced to 20 μm in diameter, the situation of the gain distribution changes greatly, and a Gaussian-like gain profile is formed. This illustrates that the increased gain may be larger than the additional thermal carrier loss, if the electric contact area is obviously reduced.

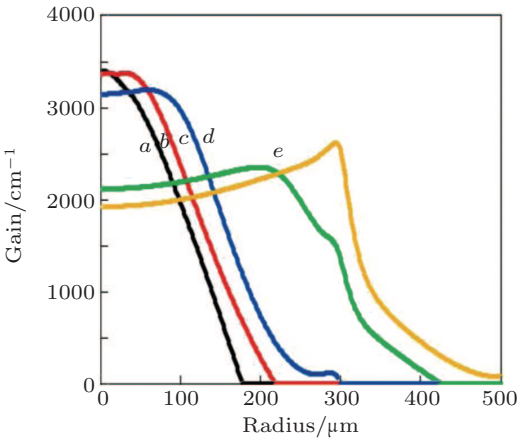


Fig. 8. (color online) Gain distributions regarding temperature effect and various p-contact diameters of 20 μm (curve *a*), 100 μm (curve *b*), 200 μm (curve *c*), 470 μm (curve *d*), and 1000 μm (curve *e*). The current aperture is 600 μm.

In addition, the gain drops to zero at $r \geq 170$ μm, in the case of the p-contact diameter of 20 μm in both Figs. 8 and 9. This is because the injected current density is too low and there is the limited carrier diffusion at $r \geq 170$ μm so that the generated gain is not enough to overcome the loss. This may be resolved by increasing the injection current.

By making the subtraction of the gains between Figs. 8 and 9 for the same electric contact sizes, the thermal carrier loss distribution from the wells due to the p-contact area or current density variation can be easily obtained. The result is shown in Fig. 10. Obviously, there are considerable thermal carrier leakages from the wells with the reduction of the contact area. As the smaller contact area leads to higher current density, the higher thermal carrier loss happens in the central zone of the active region.

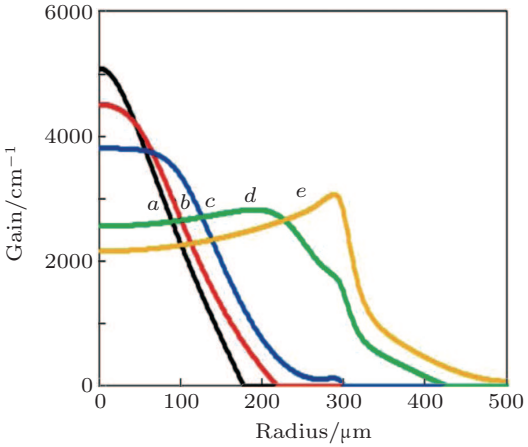


Fig. 9. (color online) Gain distributions regardless of temperature effect and with various p-contact diameters of 20 μm (curve *a*), 100 μm (curve *b*), 200 μm (curve *c*), 470 μm (curve *d*), and 1000 μm (curve *e*). The current aperture is 600 μm.

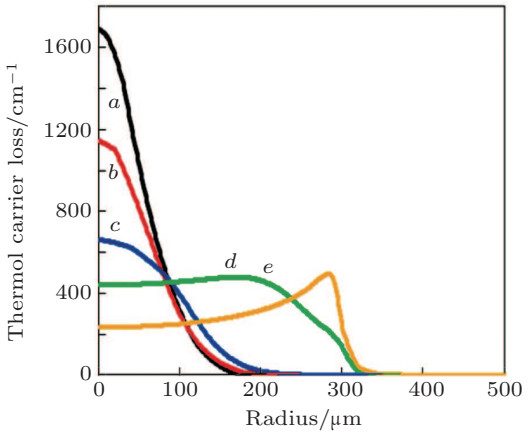


Fig. 10. (color online) Thermal carrier loss distributions in the wells for different p-contact diameters of 20 μm (curve *a*), 100 μm (curve *b*), 200 μm (curve *c*), 470 μm (curve *d*), and 1000 μm (curve *e*). The current aperture is 600 μm.

The results from Figs. 8–10 illustrate that for the broad-area bottom-emitting VCSEL, when the p-contact is small enough in comparison with the current aperture size, the gain in the central zone of the active region can be effectively increased so that it is much higher than the gain around the aperture edge, although there is the additional thermal carrier loss generated in the same zone due to the current density increase. This result is exciting, for it may increase the light emission power in the center of the active region so that the optical

near-field mode can be improved from the ring-shape to the Gaussian-like profile for the extra-broad-area VCSELs.

The mode improvement mechanism by reducing p-contact size in a broad-area bottom-emitting VCSEL which has a large current aperture is different from that of the direct use of a small current aperture in the VCSEL. For a broad-area device, the gain distribution can be easily changed in a large active region due to the contact area reduction and lateral carrier diffusion effect to improve the optical mode, while the mode improvement in a small aperture device is mainly dependent on the control of the waveguide effect because it is less effective on the gain profile change by reducing the current aperture diameter, for the active region is correspondingly reduced as well. An important point is that the use of a small current aperture in the VCSEL will cause the output power to reduce because the small aperture device has a higher carrier density and thus higher thermal carrier loss in the active region than the large aperture device under the same injection current level.

6. Conclusions

In order to improve the ring-mode situation in the extra-broad-area oxide-confined VCSEL, the gain and carrier loss distributions related to the various electric contact areas, current diffusion, and temperature effect are modeled and analyzed in detail. Since the gain and loss distributions are tightly related to the device resistance, the injection carrier diffusion and the temperature effect, an equivalent circuit network model characterizing the electric characteristics of the VCSEL is built to characterize the current diffusion. To do so, the DBR resistances which are the main heating sources in the VCSEL are calculated using the thermionic emission model and the finite difference method at first. Then, the equal potential lines and the current distribution around the active region with various p-contact areas for the bottom-emitting VCSEL are calculated by the iterative processing of the potentials for all nodes of the equivalent circuit network. The temperature variation in the radial direction due to the different current distributions caused by the p-contact area change is calculated using the steady-state thermal conduction equation and the 3D finite element method. Both temperature and current density variations show similar configurations in distribution, as the p-contact area varies in the bottom-emitting VCSEL. This is because the increase of the current density leads to higher temperature of the active region due to the ohm heating from the DBR reflectors.

The results of the current diffusion and temperature variation due to the change of the contact area are substituted into the model for the gain and thermal carrier loss profile calculations. The calculation result shows that the ring-shaped gain profile reduces in the radial direction with the reduction of p-contact area so that it is possible to obtain the Gaussian-like gain distribution when a small enough p-contact is used for the broad-area bottom-emitting VCSEL. In this case, the gain generated from the current density increase in the central zone of the active region may be larger than additional carrier loss due to the temperature effect in the same zone. Thus, this offers the possibility of improving the ring mode situation in the extra-broad-area bottom-emitting VCSEL.

References

[1] Samal N, Johnson S R, Ding D, Samal A K, Yu S Q and Zhang Y H 2005 *Appl. Phys. Lett.* **87** 161108
[2] Nakwaski W and Sarzala R P 2011 *Opt. Applicata* **41** 7
[3] Zhao Y G and McInemey J G 1996 *IEEE J. Quantum Electron.* **32** 1950
[4] Chuang H H, Biard J R, Guenter J G, Gary R J and Butler J K 2007 *IEEE J. Quantum Electron.* **43** 1028
[5] Streiff M, Witzig A, Pfeiffer M, Royo P and Fichtner W 2003 *IEEE J. Sel. Top. Quantum Electron.* **9** 879
[6] Osinski M, Smagley V A, Liu M, Smolyakov G A, Eliseev P G, Shen B P and Simonis G J 2003 *IEEE J. Sel. Top. Quantum Electron.* **9** 1422
[7] Michalzik R and Ebeling K J 1993 *IEEE J. Quantum Electron.* **29** 1963
[8] Zhang H B, Mrozynski G, Wallrabenstein A and Schrage J 2004 *IEEE J. Quantum Electron.* **40** 18
[9] Morozov V N, Neff J A and Zhou H J 1997 *IEEE J. Quantum Electron.* **33** 980
[10] Liu Y, Ng W C, Klein B and Hess K 2003 *IEEE J. Quantum Electron.* **39** 99
[11] Yu S F 2003 *IEEE J Quantum Electron.* **39** 1362
[12] Valle A 1998 *IEEE J. Quantum Electron.* **34** 1942
[13] Liu H Q, Zhang J, Cui D F, Xu Z Y, Ning Y Q, Yan C L, Qin L, Liu Y, Wang L J and Cao J L 2004 *Acta Phys. Sin.* **53** 2986 (in Chinese)
[14] He G R, Shen W J, Wang Q, Zheng W H and Chen L H 2010 *Infr. Laser Eng.* **139** 57
[15] Dutta N K 1990 *J. Appl. Phys.* **68** 1961
[16] Pinches M S, Frost J E F, Martin P M, Sale T E, Robson P N and Woodhead J 2000 *IEE Proc. Optoelectron.* **147** 11
[17] Iga K, Koyama F and Kinoshita S 1988 *IEEE J. Quantum Electron.* **24** 1845
[18] Huang M, Wu J, Cui H Y, Qian J Q and Ning Y Q 2012 *Chin. Phys. B* **21** 104207
[19] Kumar R C 1968 *Solid State Electronics* **11** 543
[20] Wu J 2006 *Acta Phys. Sin.* **55** 5848 (in Chinese)
[21] Coldren L A and Corzine S W 1995 *Diode Lasers and Photonic Integrated Circuits* (New York: John Wiley & Sons, Inc)